

Long-Lifetime Triboelectric Nanogenerator Operated in Conjunction Modes and Low Crest Factor

Xinyuan Li, Xing Yin, Zhihao Zhao, Linglin Zhou, Di Liu, Chunlei Zhang, Chuguo Zhang, Wei Zhang, Shaoxin Li, Jie Wang,* and Zhong Lin Wang*

The high-output triboelectric nanogenerator (TENG) is indispensable for its practical applications toward industrial products. However, the electricity loss in simple parallel connection among all units and the typically high crest factor output seriously hamper the practical applications of TENG. Here, a rectified TENG is reported in parallel structure to solve the problem of electricity loss in simple parallel connection. The rotational contact–separation structure with phase difference between rectified TENGs addresses high crest factor output and extends service life of rotational TENG simultaneously. The current crest factor is dramatically decreased to 1.31 in multiple rectifier multiple TENG in parallel (MRM-TENG), while that of TENG in simple parallel is higher than 6. Meanwhile, the current output can retain up to $\approx 93\%$ of its initial performance after 7 200 000 rotations under 2.00 r s^{-1} of 1000 h. Furthermore, the equivalent current can be in linear growth with low crest factor by making MRM-TENG in parallel for distributed energy supply without electricity loss. This work may provide a new strategy for TENG in parallel to achieve a low crest factor output and long-term cycling stability power generation in distributed energy harvesting for large-scale power application.

1. Introduction

Triboelectric nanogenerator (TENG), as a distinctive revolutionary technology converting low-frequency mechanical energy into electricity, has attracted tremendous interest due to its unique advantages of high peak power density, light weight,

simple design, environmental friendliness, and diverse choice of materials.^[1–9] All these merits show that TENG is a promising technology to harvest distributed energy to compensate the energy consumption of the supercapacitors/batteries and drive small electronic equipment straightforward.^[10–17]


To increase the overall power output, the contact area and structure of TENG have been widely investigated.^[4,7,18] However, it is hard to directly drive a commercial electronic equipment with high power consumption by a single TENG due to its inherent nature of low current. Thus, it is necessary to make TENGs in parallel for providing a relatively large amount of electric current as energy supply device.^[18–22] When connecting several TENGs in parallel, the intrinsic impulse alternating current signals inevitably make a huge electricity loss due to out-of-phase cancellation among of the units unless all of output signals are kept in perfect operation alignment.

Although the structure design could avoid the appearance of phase difference,^[23] it is difficult to make every single TENG keep in consistent output in harvesting biological mechanical energy, wind energy, or ocean wave energy with varying frequency and amplitude.^[18,21] So there is an urgent need to efficiently make TENG in parallel without unnecessary electricity loss.

Some works obtain the sum of every rectified output of TENG in order to avoid the electricity loss caused by waves interference, but the typically short duration pulse output of TENG has a far lower effective current than the peak value, resulting in a high crest factor (the ratio of the peak value to the effective value of current output).^[22] Generally, the crest factor of the constant direct current (DC) and the commercial alternating current (AC) is 1.00 and 1.41, respectively, which is much lower than that (6–12) of TENGs.^[22] Such typical high crest factor of TENG can seriously influence working lifetime and capacity performance in terms of driving small electronic equipment directly or acting as energy supply to charge batteries/supercapacitors.^[22] To decrease the crest factor, the conventional approaches focus on increasing the working frequency.^[18] However, it is unrealistic to directly harvest the distributed high frequency mechanical energy in the ambient for biomechanical and blue energy whose working frequency are typical

X. Li, X. Yin, Dr. Z. Zhao, Dr. L. Zhou, D. Liu, C. Zhang, C. Zhang, W. Zhang, S. Li, Prof. J. Wang, Prof. Z. L. Wang
Beijing Institute of Nanoenergy and Nanosystems
Chinese Academy of Sciences
Beijing 100083, China
E-mail: wangjie@binn.cas.cn; zhong.wang@mse.gatech.edu

X. Li, X. Yin, Dr. Z. Zhao, Dr. L. Zhou, D. Liu, C. Zhang, C. Zhang, W. Zhang, S. Li, Prof. J. Wang, Prof. Z. L. Wang
College of Nanoscience and Technology
University of Chinese Academy of Sciences
Beijing 100049, China
Prof. Z. L. Wang
School of Materials Science and Engineering
Georgia Institute of Technology
Atlanta, GA 30332, USA

 The ORCID identification number(s) for the author(s) of this article can be found under <https://doi.org/10.1002/aenm.201903024>.

DOI: 10.1002/aenm.201903024

lower than 5 Hz.^[1,15,18,24,25] A novel approach decreasing the crest factor is achieved by means of superimposing different regularly shifted phases,^[22] but its rotational sliding friction TENG mode is limited by short working lifetime. The continuous wearing between the electrode and relative friction layer in rotational sliding friction TENG mode will sharply provide a large amount of heat to damage friction material, which limits TENG's working durability and commercialization.^[2,20,26] Therefore, it is an urgent issue to simultaneously solve the problems of electricity loss of TENG in parallel, high crest factor output, and short lifetime in rotational structure of TENG.

Here, a low crest factor output and long-lifetime TENG without unnecessary electricity loss is achieved through a tactful combination of rectified TENGs in parallel with phase difference and rotational contact–separation mode. We provide a systematical simulation to reduce crest factor of wave without unnecessary electricity loss through wave interference with phase difference. Based on the results, in multiple rectifier multiple TENG in parallel (MRM-TENG), the current crest

factor is dramatically decreased to 1.31. The current output can retain up to $\approx 93\%$ of its initial performance after 7 200 000 rotations under 2.00 r s^{-1} of 1000 h contributed by the structural advantage of rotational contact–separation mode. This work may provide a new strategy for TENG to achieve a low crest factor output and long-term cycling stability power generation in distributed energy harvesting for large-scale power application.

2. Results

2.1. Design of SRM-TENG and MRM-TENG

In order to obtain a stable low crest factor output by phase difference interference wave, a design of rotational contact–separation TENG with multiple electrodes that distributed on the outside of the ring evenly is employed to convert mechanical energy into electric power. It consists of two parts, a stator and a rotor, as shown in Figure 1a. The stator is composed of

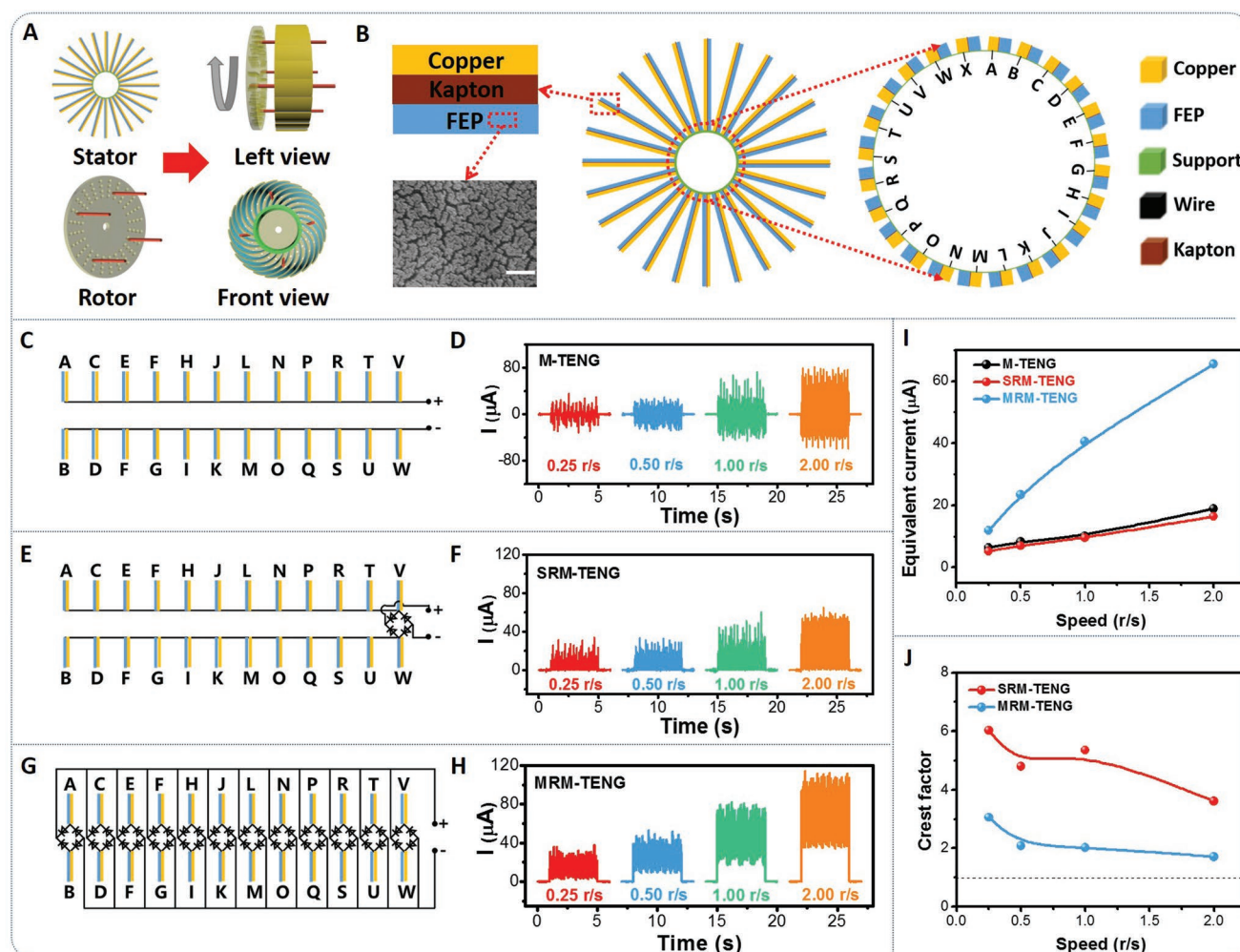


Figure 1. Design of the M-TENG, SRM-TENG, and MRM-TENG and their electrical performance. a) Schematic description of M-TENG and its detailed structure. b) Full size and enlarged detailed version of the stator in M-TENG (scale bar: 100 nm). c) Circuit and d) current outputs of M-TENG. e) Circuit and f) current output of SRM-TENG. g) Circuit and h) current output of MRM-TENG. Relationship between i) equivalent current, j) crest factor, and speed of three types of TENG, respectively.

a ring, which contains 24 electrodes, named A-X, respectively (Figure 1b). Every electrode consists of three layers in total, fluorinated ethylene propylene (FEP) dielectric layer, Kapton supporting layer, and copper conducting layer. The rotor owns just several push rods. This design tactfully achieves the contact–separation mode of TENG by rotational structure, which extends the working durability and achieves a long-term stability of rotational TENG. According to the contact–separation mode TENG (Figure S1, Supporting Information), every two adjacent electrodes form a TENG device. When the FEP and copper surfaces achieve physical contact by the rotational push rod, triboelectric charges will be created on the two contacted surfaces (I progress in Figure S1, Supporting Information). Then a potential difference can be generated when the two surfaces are separated by mechanical motion, which will drive electrons flow back and forth between the two electrodes (II, III, and IV progresses in Figure S1 in the Supporting Information). Considering the impact of different connection methods on the output of TENG, three types of circuits are discussed as shown in Figure 1c–h. Multiple TENGs in simple parallel (M-TENG) with traditional circuit mode generate AC signal which increases with rising rotational speed (Figure 1c,d). Similar to previous studies, a full-wave rectifier is added into the M-TENG circuit to form a single rectifier M-TENG (SRM-TENG) to produce DC signals (Figure 1e,f), accompanied with the similar value of equivalent current with M-TENG (I_{EC} , the quotient of the integral of current and time with respect to time

$$I_{EC} = \int_t^{t+\Delta t} I dt / \Delta t \quad (1)$$

where I is the collected experimental data and Δt is the required time, Figure 1i. Differently, when every single TENG first links with the rectifier, respectively, and then connects to the circuit in parallel to form the multiple rectifier M-TENG (MRM-TENG), the I_{EC} of MRM-TENG can boost up to 4.27-fold compared with that of SRM-TENG (Figure 1–i) (open circuit voltage, transferred charge, and detailed value of I_{EC} and crest factor of three types of TENGs are described in Figure S2 and Tables S1 and S2 in the Supporting Information). Especially, the crest factor of MRM-TENG is significantly lower than SRM-TENG (Figure 1j). For example, the crest factor can be decreased from 5.35 for SRM-TENG to 2.01 for MRM-TENG at 1.00 r s^{-1} . Taking advantage of the structure of MRM-TENG, the problems in traditional TENGs in parallel of unnecessary electricity loss and high crest factor is effectively solved. Furthermore, the output performance of two kinds of circuit structure MRM-TENG (Type I and Type II in Figure S3, Supporting Information) shows that the Type II structure can harvest more electric energy than Type I (Figure S4, Supporting Information), indicating its better harvest efficiency.

2.2. Working Mechanism of SRM-TENG and MRM-TENG

Typically, the working mechanism of the M-TENG is based on the coupling of triboelectric effect and electrostatic induction. The triboelectric charges on the surface of the electrode electrostatically induce the opposite charges on the next electrode, thereby, causing AC current among the electrodes

(Figures S1 and S2a, Supporting Information). However, SRM-TENG and MRM-TENG show different I_{EC} and crest factor because of different circuit connections. The simulation results explain the different current output shapes of SRM-TENG and MRM-TENG, as shown in Figure 2. An intermittent triangular wave is used to simulate an output signal of TENG, shown in Figure 2a, where the rest time is 0.3 s, the time of forming triangular wave is 0.2 s, and then a reverse symmetric wave is appeared, the whole period time is 1.0 s, the peak current and I_{EC} is 10 and $2 \mu\text{A}$, respectively, therefore, the crest factor is 5, which is close to the value of reported TENG. Ten separate current waves are used to simulate the output current shape of SRM-TENG and MRM-TENG mode. As shown in Figure 2b, for SRM-TENG mode, every separate wave keeps the same shape with the origin signal (Figure S5a, Supporting Information). The whole output is presented after 10 separated waves superimposing without phase difference and rectifying (Figure 2b). As presented in Figure 2c, for MRM-TENG mode, every wave-forms a bitriangular shape due to the flipping of negative part by separate rectified (Figure S5b, Supporting Information). The sum output is the interference of 10 separate rectified waves without phase difference. Thus, the same shape of SRM-TENG and MRM-TENG is obtained when the separate wave does not have phase difference. However, when the separate waves show a regular phase difference of 0.1 s, it can be seen from Figure 2d that the output current is zero for the simulated SRM-TENG. This phenomenon indicates the inevitable electricity loss of traditional TENGs in parallel if all signals are not in the same phase. Differently, the straight line at $20 \mu\text{A}$ of simulated MRM-TENG provides an opportunity to overcome the traditional high crest factor characteristic of TENG without electricity loss. In SRM-TENG, multiple groups of TENG working at different times will neutralize the positive and negative charges, resulting in electricity loss due to the principle of wave interference. In MRM-TENG, this problem has been solved by rectification first. Therefore, MRM-TENG shows a higher output without the unnecessary power loss. Next, simulation focuses on the various phase differences between 10 separated waves in wave interference of two modes, shown in Figure 2f,g (detailed current waves of simulated SRM-TENG and MRM-TENG are shown in Figures S6 and S7 in the Supporting Information). With the decrease of phase difference from 0.5 s to 0.01 s, the simulated I_{EC} of SRM-TENG decreases to the minimum value of 0 at 0.2 s and 0.1 s, and then gradually increases (Figure 2f). It is noticed that the reduction of crest factor for SRM-TENG is at the expense of sacrificing electrical energy, resulting in a lower output and even at zero (Figure 2f). On the contrary, the results of simulated MRM-TENG present that the crest factor can be decreased without electricity loss (the I_{EC} keeps $\approx 20 \mu\text{A}$ under various phase difference), and the crest factor reach to the minimum value of 1 at optimal phase difference 0.1 s (Figure 2g). This behavior is attributed to the interference of the optimal phase difference, which continuously superimposes and reduces the crest factor more effectively. Further research focuses on the influence of the wave number (device number) at optimal phase difference as shown in Figure 2h. Both the high I_{EC} and the low crest factor simultaneously of simulated MRM-TENG can be successfully achieved with the increase of device number (detailed current output is shown in Figure S8,

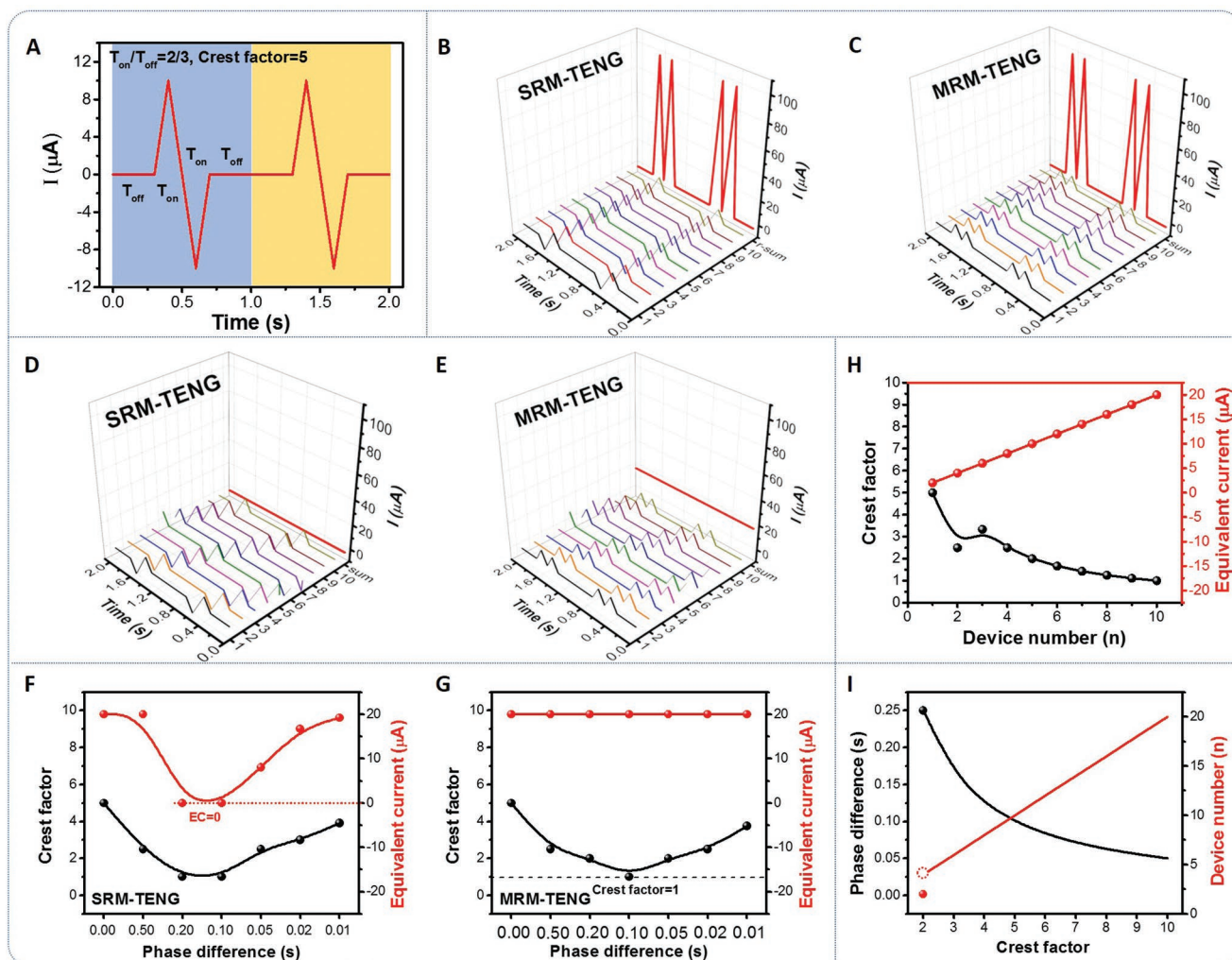


Figure 2. Working mechanism of the SRM-TENG and MRM-TENG. a) A simulated TENG signal with crest factor of 5. The interference wave under b) simulated SRM-TENG and c) simulated MRM-TENG with no phase difference. The interference wave under d) simulated SRM-TENG and e) simulated MRM-TENG mode with regular phase difference. The crest factor and equivalent current under f) simulated SRM-TENG and g) simulated MRM-TENG with various phase difference. h) The crest factor and equivalent current of MRM-TENG under different device number. i) The optimal phase difference and minimum device number of various crest factor waves to obtain the interference wave with crest factor of 1.

Supporting Information), for example, a low crest factor of 1 with high $I_{EC} \approx 20 \mu\text{A}$ is obtained when the wave number is 10. Based on this working principle, a strategy can be proposed to generate an ideal crest factor of 1 for various shapes of current wave (Figure S9, Supporting Information). Figure 2i presents the optimal phase difference and corresponding minimum device number for various kind of crest factor of TENGs to achieve an ideal crest factor of 1. For the sharp triangular wave with high crest factor ≈ 10 , it at least needs 20 devices to superimpose to achieve an output wave with crest factor ≈ 1 when the phase different is 0.05 s. Therefore, the desired values of crest factor and I_{EC} in the interference wave applied in various application field can be obtained by adjusting the phase difference and device number. According to these results, a real complex TENG wave is utilized to replace the simple triangular wave to simulate the output performance of real TENG in parallel, which shows that the low crest factor interference wave without electricity loss can also be obtained (Figure S10 and

Table S3, Supporting Information). This method provides an effective strategy of making TENG in parallel to generate a low crest factor interference wave without electricity loss in harvesting wind energy, biomechanical energy, and ocean wave energy. Therefore, inspired by the MRM-TENG working mechanism, the development of utilizing multiple rectifier circuit to enhance I_{EC} and lessen crest factor of TENG in parallel is highly desired and it pushes the electricity generation of the TENG to the next low crest factor DC stage.

2.3. Performance Optimization in MRM-TENG

MRM-TENG can produce a low crest factor interference output. Here, to optimize the output performance of the MRM-TENG, its structure, for example, electrode size, distance between push rod and electrode edge, and push rod number, is systematically studied. As shown in Figure 3a–c, the R , W , L , D and N

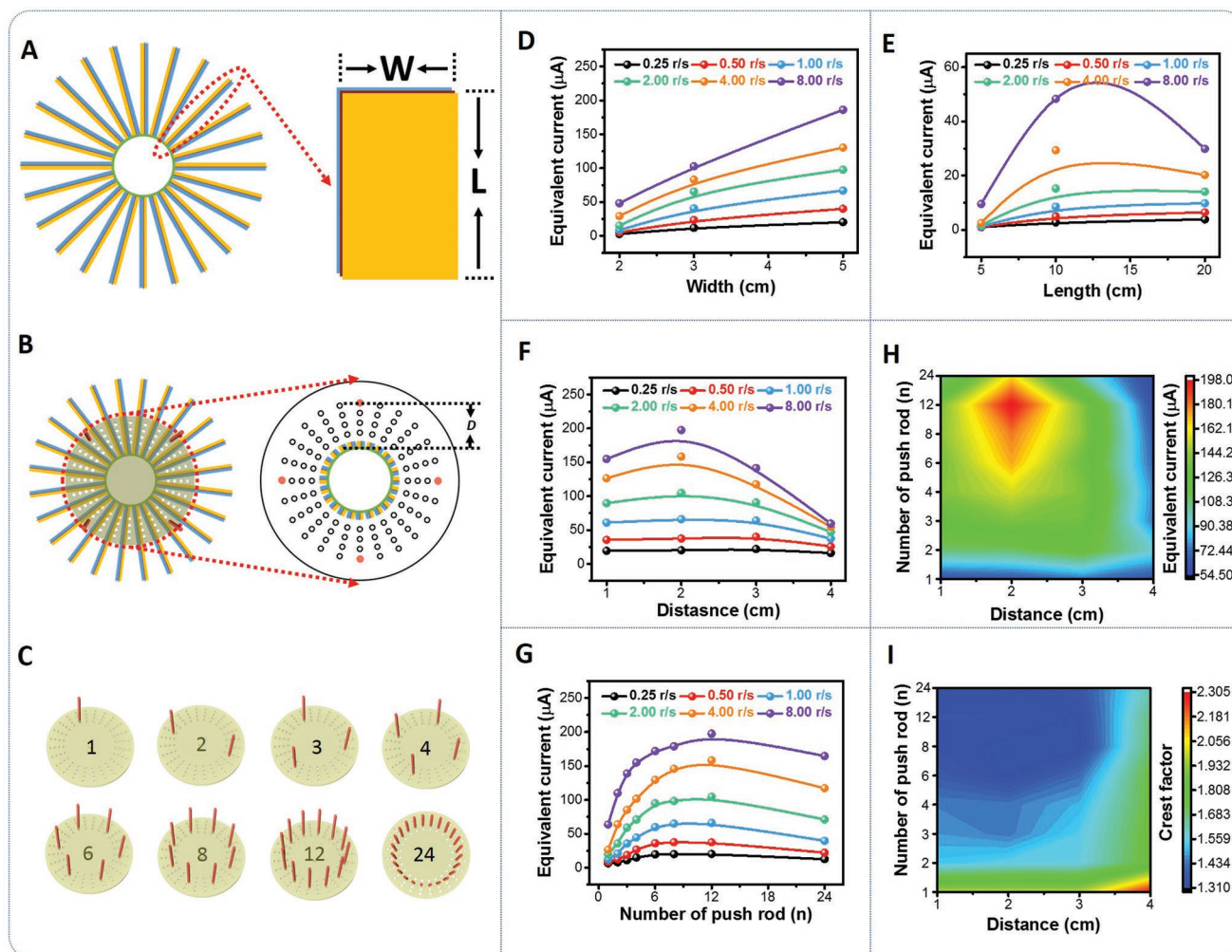


Figure 3. Performance optimization in MRM-TEG. The schematic description of a) length and width, b) distance between electrodes and push rod, and c) the number of push rod in MRM-TEG. The equivalent current performance of MRM-TEG at different parameters: d) width, where $L = 10$ cm, $D = 2$ cm, $N = 4$, e) length, where $W = 2$ cm, $D = 2$ cm, $N = 4$, f) distance between electrodes and push rod, where $L = 10$ cm, $W = 5$ cm, $N = 4$, g) the number of push rod, where $L = 10$ cm, $W = 5$ cm, $D = 2$ cm. h) The equivalent current and i) crest factor performance of MRM-TEG affected by the distance and the number of push rod, where $L = 10$ cm, $W = 5$ cm. (The speed is 8.00 r s^{-1}).

are introduced to describe the relationship between structure parameters and output performance of MRM-TEG, where R is the radius of the supporting ring, W and L are the width and length of the electrodes respectively, D is the perpendicular distance between the push rod and the electrode edge, and N is the number of the push rods. It is noticed that the I_{EC} increases as the speed rises from 0.25 to 8 r s^{-1} under different structure parameters (Figure 3d–g), and corresponding current output curves are shown in Figure S11–S14 (Supporting Information). The I_{EC} presents an approximate linear relationship with the increase of the W (Figure 3d and Figure S11, Supporting Information). With the increase of L , I_{EC} increases first and then decreases (Figure 3e and Figure S12, Supporting Information). Similarly, when the D increases, the I_{EC} also increases first and then rapidly decreases (Figure 3f and Figure S13, Supporting Information). Furthermore, depending on the number of the push rod from 1 to 24, the I_{EC} first increases and then gradually decreases (Figure 3g and Figure S14, Supporting Information).

According to the basic working principle of TENG, increasing the effective contact area is the most fundamental way to increase the I_{EC} . Considering the overlap between the adjacent electrodes in the MRM-TEG, it is unwise to increase L and decrease D blindly to improve the contact area (Figure 3e,f). A critical condition with the largest contact area is presented: the last push rod just leaves two electrodes and the next push rod just touches two electrodes during the working process of MRM-TEG. At this time, there is a quantitative relationship between the R , L , D , and N

$$\theta = \frac{2\pi}{N} \approx \frac{L-D}{R+D} \quad (2)$$

where θ is the sweeping rotation angle of each push rod. Thus, the optimal effective contact area, that is, the maximum usage of electrode contact area, is produced when θ is similar to the radian of the push rod sweeping over the electrode. When R and L

are fixed, the influence of N and D on the I_{EC} and crest factor is depicted in Figure 3h,i, showing that the appropriate N and D contribute a high equivalent current and a lower crest factor output. The I_{EC} can be boosted to ≈ 0.20 mA and the crest factor can be dramatically decreased to 1.31 by selecting appropriate parameters. The detailed relationship between different parameters is presented in Figure S15 (Supporting Information). Furthermore, different number of electrodes of MRM-TENG is fabricated to obtain more information about equivalent current and crest factor as shown in Figure S16 (Supporting Information). The MRM-TENG with 24 electrodes exhibit a higher I_{EC} with lower crest factor output than that of MRM-TENG with 12 electrodes. On account of the overlap between the electrodes, the I_{EC} of MRM-TENG with 24 electrodes increases only $\approx 50\%$ than 12 electrodes and the crest factor decreases $\approx 50\%$. Scaling up or downsizing MRM-TENG in the same proportion with optimal parameters can be used as distributed energy supply under different conditions. Such design can address the high crest factor and low equivalent current simultaneously that TENG has faced for a long time in the advanced development.

2.4. Applications of MRM-TENG

A rotational contact–separation MRM-TENG can be designed for wind energy harvester in distributed energy supply, easing the pressure of main supply during the electricity consumption peak period (Figure 4a).^[27] The push rod adding the coaxial tube reduces friction force with electrodes for a longer working lifetime of MRM-TENG. The MRM-TENG solves the bottleneck of the traditional TENG with rotation mode with short service lifetime and expands the using scope of traditional vertical contact–separation mode's TENG, which only collects mechanical energy in a single direction. In addition, it takes advantage of both the long working lifetime of the vertical contact–separation mode and harvests wind energy based on the rotational mode in any direction. As the wind speed increases, the current continuously increases and the voltage increases first and then decreases (Figure 4b–d). The I_{EC} maintains a positive correlation with wind speed. The MRM-TENG presents high output voltage of 800–1100 V and equivalent current of ≈ 0.2 mA under the speed of 8.00 r s^{-1} , respectively. As shown in Figure 4c–e and Figure S17 (Supporting Information), the stable wave of current and voltage with low crest factor is presented in a long-time cycling test, indicating an excellent performance of MRM-TENG. The current output can retain up to $\approx 93\%$ of its initial performance after 7 200 000 rotations under 2.00 r s^{-1} of 1000 h and the phase structure of copper electrode and FEP is unchanged after the cycling (Figure S18, Supporting Information). The reality of wind power system is typical rotation of 0.50 – 1.00 r s^{-1} . The relatively high speed of 2.00 r s^{-1} is used for the accelerated stability test. The result means that the MRM-TENG will have better working durability performance in actual application. Such an MRM-TENG is also a proper energy supply to charge a lithium ion battery (Figure S19, Supporting Information). It takes 1.8 h to make the lithium ion battery obtain capacity of 153 μAh and the coulombic efficiency reaches up to 94.6%. Meanwhile, current shape and average power under different loads are also studied

in detail in Figure 4f,g, and Figures S20 and S21 (Supporting Information). The MRM-TENG exhibits a maximum average power of ≈ 18 mW at a matched load resistance of $10 \text{ M}\Omega$ and possesses volumetric power of 36 W m^{-3} . The electrode of MRM-TENG only weighs on the order of gram, far below than mainstream wind generator. The mass specific power of MRM-TENG is $\approx 400 \text{ W kg}^{-1}$. The equivalent current can be in linear growth with low crest factor by making MRM-TENG in parallel (Figure 4h). Furthermore, MRM-TENG possesses low cost and flexible size compared with electromagnetic wind generator, which can be industrialized to harvest distributed energy in some environments (Figure 4i).^[28,29] In practical applications, even if some electrodes are damaged during long-term operation, MRM-TENG can still work due to independent electrode structure. Compared with the conventional rotational free-standing TENG, its working durability has been greatly improved (Figure S24, Supporting Information). Such design may provide a new strategy for TENG to achieve a low crest factor and long-term cycling stability power generation in distributed energy harvesting for large-scale power application.

3. Conclusion

In summary, our work solves several problems of electricity loss of the TENGs in simple parallel connection, inherent high crest factor output of TENG, and short working lifetime of TENG basing on rotational structure. To be specific, rectified TENG in parallel prevents the unnecessary electricity loss; phase difference between several rectified TENG addresses the high crest factor output; the rotational contact–separation mode provides a powerful approach for a long-term stability lifetime. Therefore, a low crest factor and long-term stability output of MRM-TENG is obtained simultaneously without unnecessary electricity loss. The simulation results present the working mechanism that the desired value of crest factor and equivalent current in wave interference can be obtained by adjusting the phase difference and device numbers. As inspired by the MRM-TENG working mechanism, the development of utilizing multiple rectifier circuit to enhance equivalent current and lessen crest factor of TENG in parallel is highly desired and it the electricity generation of the TENG to the next low crest factor DC stage. Meanwhile, the challenge of how to manipulate multiple electrodes and correlate structure details to improve device performance have been well discussed. The current crest factor is dramatically decreased to 1.31 in MRM-TENG. The equivalent current can be in linear growth with low crest factor by making MRM-TENG in parallel for distributed energy supply without electricity loss. The efficiency can retain up to $\approx 93\%$ of its initial performance after 7 200 000 rotations under 2.00 r s^{-1} of 1000 h. This work may provide a new strategy for TENG to achieve a low crest factor and long-term cycling stability power generation in distributed energy harvesting for large-scale power application.

4. Experimental Section

Fabrication of Multiphase Electrodes Triboelectric Nanogenerator. The M-TENG was composed of two parts, a stator and a rotator. The stator was constituted of multiple electrodes with the radius of 4 cm

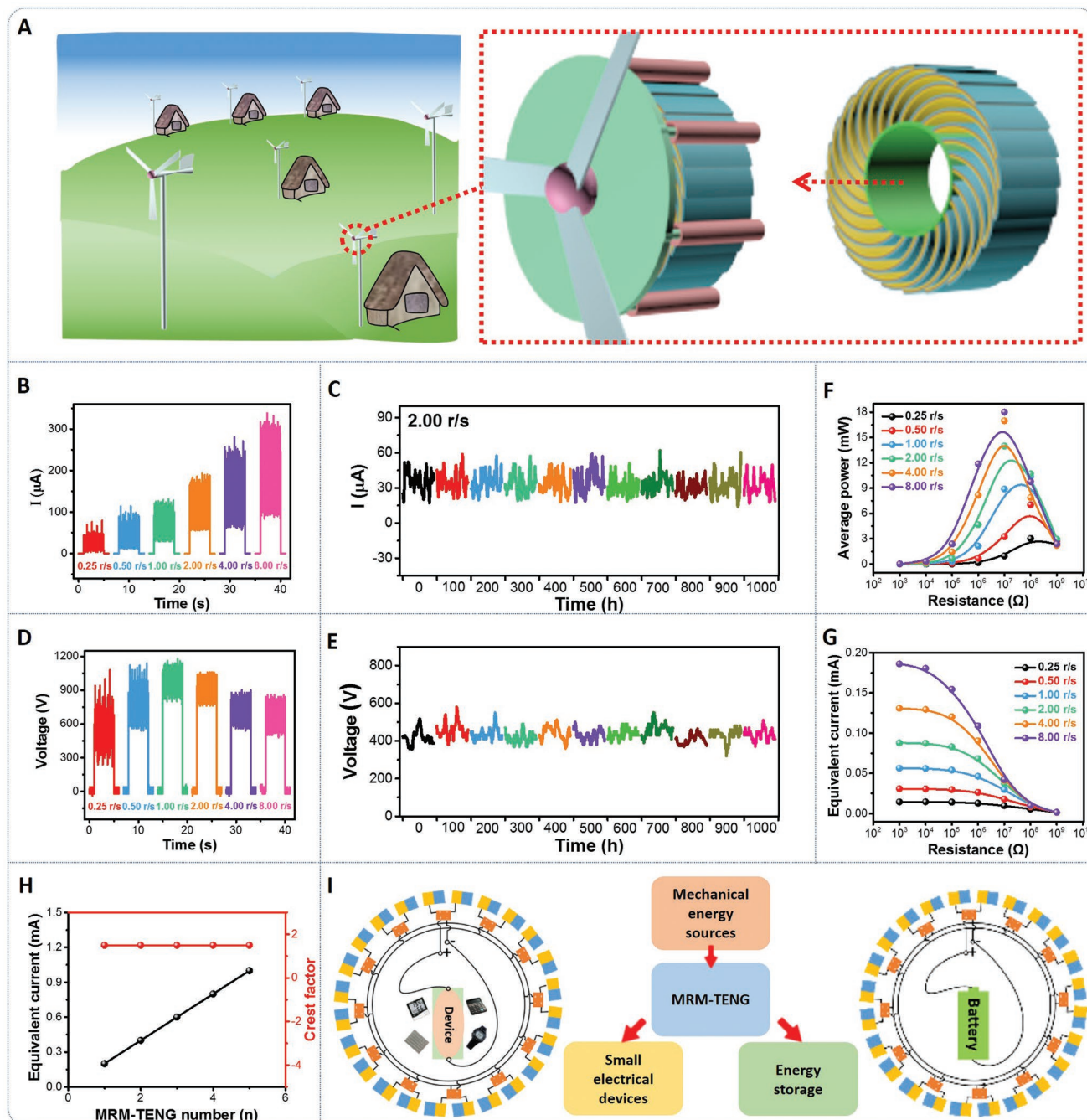


Figure 4. The application of MRM-TENG. a) The schematic description of MRM-TENG in harvesting wind energy and its application. b) The current and d) voltage output of MRM-TENG under different speeds. c) The current and e) voltage output of MRM-TENG under 2.00 r s^{-1} in a long-term stability. f) The average power and g) equivalent current of MRM-TENG under various speeds and loads. h) The equivalent current and crest factor of MRM-TENG under different device numbers. i) The schematic diagram of MRM-TENG in practical application.

each. The M-TENG had 12 TENGs constituted by 24 independent electrodes. The width of electrode was 2, 3, and 5 cm, respectively, and the length of electrode was 5, 10, and 20 cm, respectively. The electrode was consisted of FEP, copper components oppositely mounted onto a Kapton substrate using an adhesion layer. The rotator only consisted of several push rods. The push rod number was 1–24 and the distance between push rod and electrode edge was 1, 2, 3, and 4 cm.

Simulation of Outputs: The output signal of TENG was simulated by ORIGIN software based on the principle of wave interference.

To visualize the difference between the SRM-TENG and MRM-TENG, the waveform of the TENG was simplified to a triangular wave, where the rest time was 0.3 s, the time of forming triangular wave was 0.2 s, and then a reverse symmetric wave appeared, the whole period time was 1.0 s, the peak current and I_{EC} was 10 and 2 μA , respectively.

Structure Characterization: The microstructures of samples were conducted by a cold field emission scanning electron microscope (FESEM, HITACHI SU8200) with the working voltage and current of 5 kV and 10 μA , respectively. The crystalline structure of samples was

identified on a X'Pert3 diffractometer (PANalytical, Netherlands) with a Cu $K\alpha$ radiation source ($\lambda = 1.54056 \text{ \AA}$) over the range of 10° – 80° (2θ) with a step size of 0.013° , the accelerating voltage and current were 40 kV and 40 mA, respectively.

Electrochemical Characterization: The programmable electrometer (Keithley model 6514) was adopted to test the short-circuit current of TENG and to monitor the voltage in process of TENG charging lithium ion battery. A mixed domain oscilloscope (MDO3024) was used to test the open-circuit voltage. A rotational motor (HBS86H) was applied to drive the M-TENG, SRM-TENG, and MRM-TENG. Galvanostatic discharge tests of cells were carried out on a LAND CT2001A system (Wuhan, China).

Supporting Information

Supporting Information is available from the Wiley Online Library or from the author.

Acknowledgements

X.L., X.Y., and Z.Z. contributed equally to this work. Research was supported by the National Key R&D Project from Minister of Science and Technology (grant no. 2016YFA0202704), National Natural Science Foundation of China (grant nos. 61774016, 51432005, 5151101243, 51561145021), and Beijing Municipal Science & Technology Commission (grant nos. Z171100000317001, Z171100002017017, Y3993113DF). Patents were filed based on the research results presented in this manuscript.

Conflict of Interest

The authors declare no conflict of interest.

Keywords

crest factor, phase difference, triboelectric nanogenerators

Received: September 15, 2019

Revised: November 14, 2019

Published online:

- [1] Z. L. Wang, *Nature* **2017**, *542*, 159.
- [2] Z. L. Wang, *Mater. Today* **2017**, *20*, 74.
- [3] Z. L. Wang, *Nano Energy* **2018**, *54*, 477.
- [4] J. Wang, C. S. Wu, Y. J. Dai, Z. H. Zhao, A. Wang, T. J. Zhang, Z. L. Wang, *Nat. Commun.* **2017**, *8*, 88.
- [5] Z. L. Wang, *Nano Energy* **2019**, *58*, 669.
- [6] H. Y. Guo, X. J. Pu, J. Chen, Y. Meng, M. H. Yeh, G. L. Liu, Q. Tang, B. D. Chen, D. Liu, S. Qi, C. S. Wu, C. G. Hu, J. Wang, Z. L. Wang, *Sci. Rob.* **2018**, *3*, eaat2516.
- [7] W. L. Liu, Z. Wang, G. Wang, G. L. Liu, J. Chen, X. J. Pu, Y. Yi, X. Wang, H. Y. Guo, C. G. Hu, Z. L. Wang, *Nat. Commun.* **2019**, *10*, 1426.
- [8] C. S. Wu, W. B. Ding, R. Y. Liu, J. Y. Wang, A. C. Wang, J. Wang, S. M. Li, Y. L. Zi, Z. L. Wang, *Mater. Today* **2018**, *21*, 216.
- [9] H. S. Boudet, *Nat. Energy* **2019**, *4*, 446.
- [10] D. Gielen, F. Boshell, D. Saygin, *Nat. Mater.* **2016**, *15*, 117.
- [11] Y. L. Zi, J. Wang, S. H. Wang, S. M. Li, Z. Wen, H. Y. Guo, Z. L. Wang, *Nat. Commun.* **2016**, *7*, 216.
- [12] G. Z. Yang, J. Bellingham, P. E. Dupont, P. Fischer, L. Floridi, R. Full, N. Jacobstein, V. Kumar, M. Mcnutt, R. Merrifield, B. J. Nelson, B. Scassellati, M. Taddeo, R. Taylor, M. Veloso, Z. L. Wang, R. Wood, *Sci. Rob.* **2018**, *3*, eaar7650.
- [13] S. Chu, A. Majumdar, *Nature* **2012**, *488*, 294.
- [14] Z. R. Liu, J. H. Nie, B. Miao, J. D. Li, Y. B. Cui, S. Wang, X. D. Zhang, G. R. Zhao, Y. B. Deng, Y. H. Wu, Z. Li, L. L. Li, Z. L. Wang, *Adv. Mater.* **2019**, *31*, 1807795.
- [15] K. Dong, Z. Y. Wu, J. A. Deng, A. C. Wang, H. Y. Zou, C. Y. Chen, D. M. Hu, B. H. Gu, B. Z. Sun, Z. L. Wang, *Adv. Mater.* **2018**, *30*, 1804944.
- [16] C. S. Wu, A. C. Wang, W. B. Ding, H. Y. Guo, Z. L. Wang, *Adv. Energy Mater.* **2019**, *9*, 1802906.
- [17] X. D. Wang, J. H. Song, J. Liu, Z. L. Wang, *Science* **2007**, *316*, 102.
- [18] J. Wang, S. Li, F. Yi, Y. Zi, J. Lin, X. Wang, Y. Xu, Z. L. Wang, *Nat. Commun.* **2016**, *7*, 12744.
- [19] S. H. Wang, L. Lin, Z. L. Wang, *Nano Lett.* **2012**, *12*, 6339.
- [20] G. Zhu, J. Chen, T. J. Zhang, Q. S. Jing, Z. L. Wang, *Nat. Commun.* **2014**, *5*, 3426.
- [21] Z. Wen, M. H. Yeh, H. Y. Guo, J. Wang, Y. L. Zi, W. D. Xu, J. N. Deng, L. Zhu, X. Wang, C. G. Hu, L. P. Zhu, X. H. Sun, Z. L. Wang, *Sci. Adv.* **2016**, *2*, e1600097.
- [22] H. Ryu, J. H. Lee, U. Khan, S. S. Kwak, R. Hinchet, S. W. Kim, *Energy Environ. Sci.* **2018**, *11*, 2057.
- [23] C. L. Zhao, Q. Zhang, W. L. Zhang, X. Y. Du, Y. Zhang, S. B. Gong, K. L. Ren, Q. J. Sun, Z. L. Wang, *Nano Energy* **2019**, *57*, 440.
- [24] X. Y. Li, J. Tao, X. D. Wang, J. Zhu, C. F. Pan, Z. L. Wang, *Adv. Energy Mater.* **2018**, *8*, 1800705.
- [25] F. Yi, X. F. Wang, S. M. Niu, S. M. Li, Y. J. Yin, K. R. Dai, G. J. Zhang, L. Lin, Z. Wen, H. Y. Guo, J. Wang, M. H. Yeh, Y. L. Zi, Q. L. Liao, Z. You, Y. Zhang, Z. L. Wang, *Sci. Adv.* **2016**, *2*, e1501624.
- [26] K. Sayfidinov, S. D. Cezan, B. Baytekin, H. T. Baytekin, *Sci. Adv.* **2018**, *4*, eaau3808.
- [27] M. R. Davidson, D. Zhang, W. M. Xiong, X. L. Zhang, V. J. Karplus, *Nat. Energy* **2016**, *1*, 16086.
- [28] R. Wiser, K. Jenni, J. Seel, E. Baker, M. Hand, E. Lantz, A. Smith, *Nat. Energy* **2016**, *1*, 16135.
- [29] J. K. Lundquist, K. K. DuVivier, D. Kaffine, J. M. Tomaszewski, *Nat. Energy* **2019**, *4*, 251.